AGU100 ADVANCING EARTH AND SPACE SCIENCE

JGR

Journal of Geophysical Research: Solid Earth

RESEARCH ARTICLE

10.1029/2018JB015872

Special Section:
Gas Hydrate in Porous Media: Linking Laboratory and Field Scale Phenomena

Impact of Pore Fluid Chemistry on Fine-Grained Sediment Fabric and Compressibility

Junbong Jang[1], Shuang C. Cao[2], Laura A. Stern[3], Jongwon Jung[2,4], and William F. Waite[1]

[1]U.S. Geological Survey, Woods Hole, MA, USA, [2]Civil and Environmental Engineering, Louisiana State University, Baton Rouge, LA, USA, [3]U.S. Geological Survey, Menlo Park, CA, USA, [4]School of Civil Engineering, Chungbuk National University, Cheongju, South Korea

Key Points:

- The liquid limit-based electrical sensitivity index indicates the extent to which sediment compressibility depends on pore fluid chemistry
- Pore fluid chemistry influences initial void ratio, as observed in sedimentation and consolidation tests, and thus affects compressibility
- Pore fluid chemistry changes occur when extracting methane from hydrate-bearing sediments, potentially altering in situ compressibility

Correspondence to:
J. Jang,
jjang@usgs.gov

Citation:
Jang, J., Cao, S. C., Stern, L. A., Jung, J., & Waite, W. F. (2018). Impact of pore fluid chemistry on fine-grained sediment fabric and compressibility. *Journal of Geophysical Research: Solid Earth*, *123*, 5495–5514. https://doi.org/10.1029/2018JB015872

Received 2 APR 2018
Accepted 18 JUN 2018
Accepted article online 26 JUN 2018
Published online 17 JUL 2018

Abstract Fines, defined here as grains or particles, less than 75 μm in diameter, exist nearly ubiquitously in natural sediment, even those classified as coarse. Macroscopic sediment properties, such as compressibility, which relates applied effective stress to the resulting sediment deformation, depend on the fabric of fines. Unlike coarse grains, fines have sizes and masses small enough to be more strongly influenced by electrical interparticle forces than by gravity. These electrical forces acting through pore fluids are influenced by pore fluid chemistry changes. Macroscopic property dependence on pore fluid chemistry must be accounted for in sediment studies involving subsurface flow and sediment stability analyses, as well as in engineered flow situations such as groundwater pollutant remediation, hydrocarbon migration, or other energy resource extraction applications. This study demonstrates how the liquid limit-based electrical sensitivity index can be used to predict sediment compressibility changes due to pore fluid chemistry changes. Laboratory tests of electrical sensitivity, sedimentation, and compressibility illustrate mechanisms linking microscale and macroscale processes for selected pure, end-member fines. A specific application considered here is methane extraction via depressurization of gas hydrate-bearing sediment, which causes a dramatic pore water salinity drop concurrent with sediment being compressed by the imposed effective stress increase.

1. Introduction

Changes in the pore fluid chemistry of sediments occur in a broad range of processes. Accounting for sediment responses to changes in pore fluid chemistry is important for assessing compressibility, mechanical instability, and permeability changes during fluid flow through naturally occurring water-bearing sediment (Andersson-Skold et al., 2005; Austad et al., 2008; Frederick & Buffett, 2015; Kopf et al., 2010; Sultan et al., 2004), as well as in a range of intentionally induced pore fluid replacement applications such as oil or gas extraction (Mohan et al., 1993), extraction of methane from gas hydrate (Mohan et al., 1993; Oyama et al., 2016), CO_2 sequestration (Pudlo et al., 2015), and the remediation of nonaqueous phase liquids, or other groundwater contaminants (Glass et al., 2000; LeBlanc et al., 1991; Mackay & Cherry, 1989; Rao et al., 1997).

Fluid replacement induces changes in the pore fluid chemistry that can affect fabric formed by fine-grained particles (fines). Fines here are defined by the particles smaller than 75 μm based on ASTM D2487 (2011a) for engineering purposes, but the maximum particle size criteria for fines vary from 60 to 75 μm based on the chosen standards (Holtz et al., 2011; Jang & Santamarina, 2016). In general, when the particle size is less than 1 μm or the specific surface is greater than 25m^2/g, the gravitational influence is weak, and electrical forces due to surface charges on the particle control the arrangement or fabric of particles (Lambe & Whitman, 1969). Electrical interparticle interactions consist of attractive and repulsive electrical forces, and for particles in contact with fluid, several particle behavior models have been proposed (refer to Appendix A for detailed equations):

1. Derjaguin-Landau-Verwey-Overbeek theory combines the forces of van der Waals (VDW) attraction and diffuse double layer (DDL) repulsion (Derjaguin & Landau, 1941; Israelachvili, 2011; Mitchell & Soga, 2005; van Olphen, 1977; Verwey et al., 1948). Van der Waals attraction is due to a set of short-range electrical interactions between molecules separated by ~10 nm or less (Hu et al., 1999; Meade, 1964; Valle-Delgado et al., 2005). The DDL thickness, ϑ (m), expands and shrinks based on the ionic concentration, c_0 (mol/L; Figures 1a and 1b), and the relative permittivity of the pore fluid, κ', according to (Israelachvili, 2011; Mitchell & Soga, 2005; van Olphen, 1977)

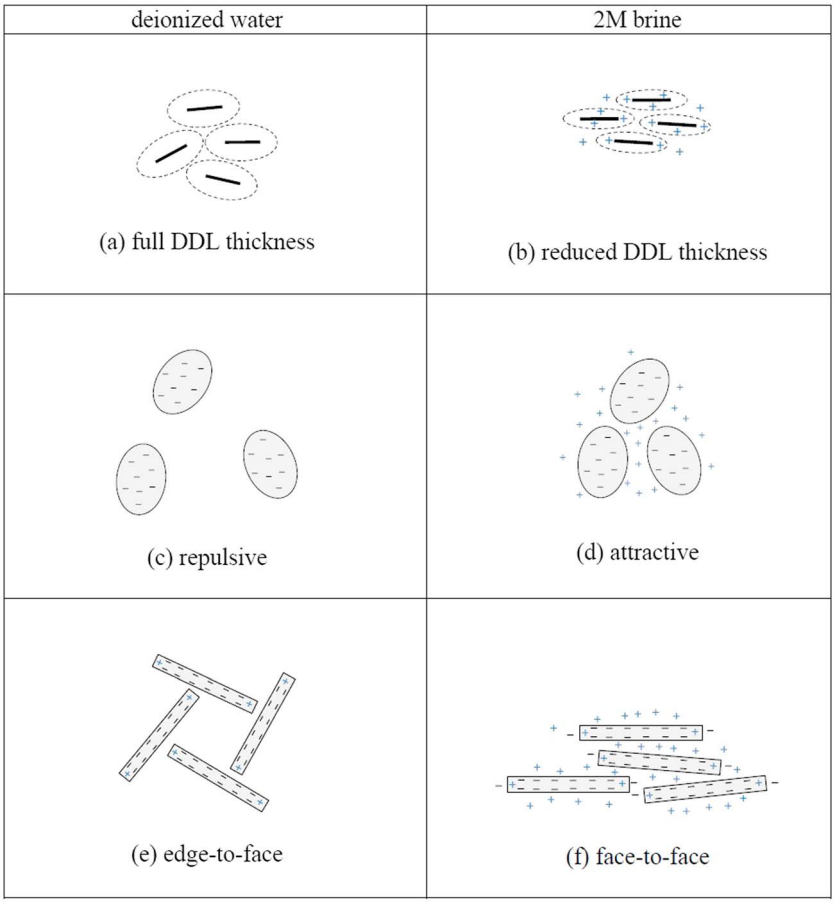

Figure 1. Mechanisms of electrical interactions among particles: (a) fully developed diffuse double layer, DDL, in deionized water and (b) reduced DDL in brine: solid lines are particles, and dashed ellipsoids are imaginary DDLs. The Sogami-Ise model shows repulsive and attractive forces due to surface charge interactions (c) between like-charged particles and (d) between particles and ions in surrounding fluid (McBride & Baveye, 2002; Sogami & Ise, 1984). Attractive interactions due to localized surface charge: (e) edge-to-face fabric and (f) face-to-face fabric. The transition for kaolin occurs between 0.01 M and 0.1 M, depending on surface charge conditions (Mitchell & Soga, 2005; Santamarina et al., 2001).

$$\vartheta \propto \sqrt{\frac{\kappa'}{c_0}}. \tag{1}$$

The full equation for equation (1) provided in Appendix A is valid in cases where the particle thickness is thin compared to the DDL thickness, and the particle possesses a high surface charge density such as montmorillonite in solution with low c_0 (less than 100 mol/m^3) of monovalent electrolyte (Mitchell & Soga, 2005; Sposito, 1989). Clays such as montmorillonite can develop DDL ~100 nm in distilled water (Mojid & Cho, 2006).

2. The Sogami-Ise model is based on Coulombic forces between like and unlike charges. In a fluid with ions, such as brine, Coulombic repulsion can be offset by the mutual attraction of neighboring particles to counter ions present in the fluid between those particles, reducing interparticle separations (compare Figures 1c and 1d; Langmuir, 1938; McBride & Baveye, 2002; Mitchell & Soga, 2005; Sogami & Ise, 1984).
3. The localized surface charge distributions on the particle surface can affect fabric formation of platy particles due to Coulombic attraction (Figures 1e and 1f; Lambe & Whitman, 1969; Mitchell & Soga, 2005; Santamarina et al., 2001).

The models suggest that changes in pore fluid chemistry parameters such as ionic concentration and permittivity will affect the electrical interactions among particles that can form different types of fines clusters and

Table 1
Material Description: Physical and Index Properties of Fines in This Study

No.	Sediment	Specific gravity G_s[a]	Median particle size D_{50} [μm]	Specific surface S_s [m^2/g][c]	Liquid limit (uncorrected)			Plastic limit PL_{DW}[d]	Plasticity index $PI = LL\text{-}PL$	Electrical sensitivity Soil classification[e]	Sedimentation test - dry mass at loose packing [g][f]
					LL_{DW}	LL_{brine}	LL_{ker}				
1	silica silt	2.65[b]	10.5[b]	0.2[g]	31	31	36	30	1	LI	9.13
2	mica	2.82[b]	17[b]	4.2	94	81	110	80	14	HI	3.59
3	$CaCO_3$	2.73	8[b]	0.2[g]	25	23	31	17	8	NI	9.87
4	diatoms	2.23	10[b]	98	119	111	140	98	21	HI	2.90
5	kaolin	2.68	4	24	77	55	83	38	39	II	5.57
6	illite	2.71	20	29	56	52	59	32	24	IL	10.49
7	bentonite	2.53	< 2[h]	579	288	126	65	54	234	HH	9.71

[a]Density analysis by gas pycnometer. [b]Data from manufacturer. [c]Water-based methylene blue test (Santamarina et al., 2002). [d]The smallest water content for plastic solid state, measured according to ASTM-D4318 (ASTM, 2005). [e]Indicating no (N), low (L), intermediate (I), or high (H) plasticity fine grains of low (L), intermediate (I), or high (H) electrical sensitivity in Figure 4. [f]Sample mold size: 25.4 mm in diameter and height. [g]Analytical calculation based on spherical particle shape. [h]Approximated value from literature (Arnott, 1965).

fabrics (Bennett & Hulbert, 1986; Lambe & Whitman, 1969; Palomino & Santamarina, 2005; Pierre & Ma, 1999). As presented in this study, the clustering and fabric formation behavior of fines due to their sensitivity to pore fluid chemistry can be anticipated by the electrical sensitivity, S_E, which can be measured with a series of liquid limit index property tests (Jang & Santamarina, 2016, 2017).

Macroscale sediment properties such as permeability, strength, and compressibility will vary based on how the pore fluid chemistry alters the microscale fabric (Bennett et al., 1989; Bolt, 1956; Chen et al., 2000; Di Maio & Fenelli, 1994; Fernandez & Quigley, 1985; Moore & Mitchell, 1974; Olson & Mesri, 1970; Quirk & Schofield, 1955; Sridharan & Rao, 1973). Even in coarse grain-dominated sediments, changes in the fabric of fines can be critical since the fine fraction can control the overall physical behavior of the sediments even at low fines concentrations. The effective fines fraction varies depending on the physical phenomena, but, for example, approximately 5% fraction of fines is enough to control the hydraulic conductivity in a sandy sediment (Bandini & Sathiskumar, 2009; Carraro et al., 2009; Hyodo et al., 2017; Kenney, 1977; Lade & Yamamuro, 1997; Park & Santamarina, 2017). This study uses the electrical sensitivity of end-member fines to link pore fluid chemistry changes to alterations in fabric formation and compressibility of a broad range of fines and pore fluid chemistries.

2. Experimental Methods

This work is based on three types of experiments. Initially, electrical sensitivity studies suggested by Jang and Santamarina (2016, 2017) are applied to classify the end-member fines in this study. The three pore fluids used for the electrical sensitivity test, deionized water, 2 M-brine (2 mol of sodium chloride, NaCl, per liter of deionized water), and kerosene, are also used in the sedimentation and consolidation tests. Sedimentation tests in a suite of pore fluid chemistries are then run on the end-member sediments, providing insights into interparticle forces relevant to each end-member sediment. Finally, consolidation tests are run for each end-member sediment saturated with deionized water, 2 M-brine, or kerosene to quantify the impact of pore fluid ionic concentration and permittivity on the compressibility of the sediment. These compressibility results are analyzed in light of the electrical sensitivity and the particle behavior observed in the sedimentation tests.

2.1. Materials

The selected end-member sediments cover a wide range of material properties, physical morphologies, and chemical compositions. The chosen sediments were crushed silica silt (quartz, SiO_2), muscovite mica (denoted in this study simply as mica), crushed calcium carbonate ($CaCO_3$), diatoms (siliceous microfossils), kaolin (primarily kaolinite), illite, and bentonite (primarily montmorillonite; Table 1). Of these, silt-size silica, mica, kaolinite, illite, and smectite (the clay group that includes montmorillonite) are common in onshore and offshore sediments, while diatoms and organic calcium carbonate in the form of microfossils are frequently found in marine sediments (Anderson et al., 2014; Bahk et al., 2013; Egawa et al., 2015; Petschick et al., 1996; Sun & Turchyn, 2014; Wiemer et al., 2017; Winters et al., 2011). Pore fluids used in the

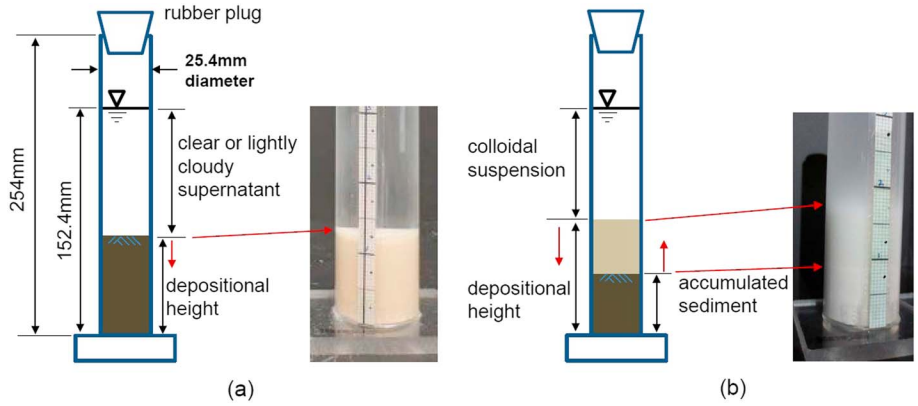

Figure 2. Height measurements observed in sedimentation tests: (a) a uniform sedimentation response in which essentially all sediment particles fall together such that a sharp interface is observed at the depositional height between the sediment and overlying clear or lightly cloudy supernatant; (b) a segregated sedimentation response in which the sediment segregates (due to different falling velocities of individually sized and clustered particles) into a bottom layer containing the largest particles (accumulated sediment), a middle layer extending to the depositional height and containing smaller particles, and an overlying cloudy colloidal suspension containing the finest particles. The directions in which the interfaces move are given by the vertical red arrows.

sedimentation tests were selected to examine the effect of ionic concentration and permittivity on interparticle interactions: deionized water (DW), brines of 0.001 M, 0.01 M, 0.1 M, 0.6 M (typical seawater), 1 M, and 2 M NaCl concentrations, 0.0654 M sodium hexamethaphosphate $(NaPO_3)_6$ solution (fine particle dispersant; 40 g/L, as suggested by ASTM D422; ASTM, 2007), and kerosene (nonpolar, low permittivity). The fluid pH during each test was approximately 7.

2.2. Electrical Sensitivity Characterization

Liquid limit-based electrical sensitivity tests were performed on each sediment to assess alterations in electrical interactions between fines in response to the fluid permittivity and electric conductivity, which itself is related to the ionic concentration (Jang & Santamarina, 2016). The electrical sensitivity of sediment is defined in terms of its liquid limit measured for deionized water, 2 M-brine, and kerosene: LL_{DW}, LL_{brine}, and LL_{ker}. Liquid limits, measured using the standard cone penetrometer method BS 1377 (BSI, 1990), define the water content for which a sediment transitions from a plastic solid to a liquid state. In addition to aiding in the electrical sensitivity characterization, liquid limits are themselves useful through their relationships to other physical properties such as hydraulic conductivity and compressibility of remolded soils (Carrier & Beckman, 1984; Lee et al., 2005; Sridharan & Nagaraj, 2000; Wroth & Wood, 1978).

2.3. Sedimentation Test

Sedimentation tests in different pore fluids provide insights into the particle arrangement or fabric due to pore fluid chemistry (Palomino & Santamarina, 2005; Pierre & Ma, 1999). Beginning with oven-dried specimens, a measured mass of sediment was spooned in ambient air into an acrylic mold to form a specimen 25.4 mm in height and diameter. This approach created a loose sediment fabric (maximum void ratio). The sediment was then mixed with a fluid to a final height of 152.4 mm to obtain a ratio of 1 to 6 in the diameter to height of the fluid column. The following fluids were used: deionized water, the various brine concentrations, 0.0654 M $(NaPO_3)_6$ solution, and kerosene. Prior to testing, a given sediment-fluid mixture was allowed to stabilize for more than 12 hr. After stabilization, the fluid cylinder headspace was vacuumed to draw gas bubbles and dissolved gas out of the fluid. The headspace was then briefly opened to the atmosphere before a stopper was sealed into the cylinder end. The cylinder was shaken for 1 min before being left to settle undisturbed. The side friction and boundary effects on the cylinder wall are considered negligible for this cylinder geometry, the volume of sediment and zero vertical effective stress (ASTM D4254, 2000). Heights of the depositional interface and the accumulated sediment interface defined in Figure 2 were measured as functions of time until the interface locations did not change (1 to 4 days).

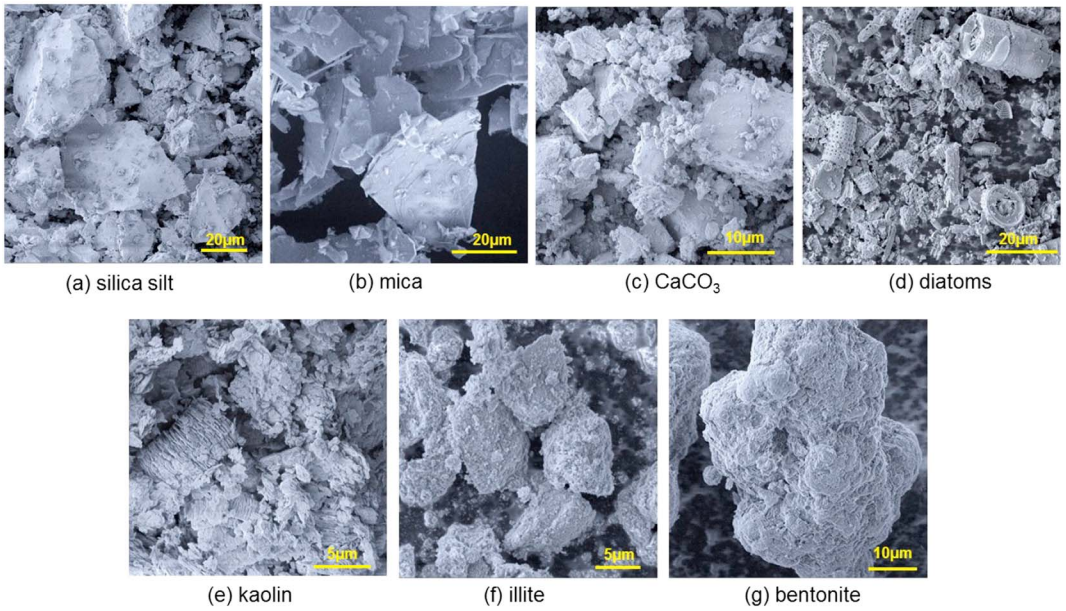

Figure 3. Scanning electron microscope, SEM, images of sediments tested in this study. (a) Silica silt, (b) mica, (c) $CaCO_3$, (d) diatoms, (e) kaolin, (f) illite, and (g) bentonite.

2.4. Consolidation Test

Incremental loading consolidation tests were conducted in a one-dimensional fixed-ring oedometer cell as described in ASTM D2435 (ASTM, 2011b) to evaluate the compressibility of end-member sediment in each pore fluid. Each specimen was mixed with pore fluid (deionized water, 2 M-brine, or kerosene) and stabilized for 12 hr before being placed in a rigid consolidation ring of 63.5-mm diameter and either 19.05 or 25.4-mm height. The initial fluid content of the specimen while setting up the oedometer for each consolidation was 1.2LL, where the liquid limit, LL, was determined from the cone penetrometer tests. The specimen was then fully submerged in the reservoir filled with pore fluid for the consolidation test. The applied vertical stress schedule was (1) loading in eight steps from 20 to 1280 kPa, doubling the load with each step; (2) unloading to 640, 160, and 40 kPa; and (3) finally reloading from 80 to 1280 kPa, again doubling the loading stress at each step. Each step was allowed to progress until there was a plateau in the displacement curve.

3. Experimental Results and Discussion

3.1. Particle Shapes

Scanning electron microscope, SEM, images in Figure 3 show the physical morphology of each sediment. Silica silt and $CaCO_3$ exhibit angular, bulky particle shapes, with smaller particles sitting on larger particles. Diatoms are siliceous microfossils often found in broken pieces that reveal the diatom's inner porosity. The diatom structure leads to high specific surface and high liquid limit, but low plasticity index, PI, which defines the water content range of the plastic state of the sediment (Table 1). Mica, kaolin, illite, and bentonite are platy phyllosilicate particles. They all show high specific surface and high liquid limit values, but mica has a relatively low plasticity index. Mica and illite have smaller particles sitting on larger particles (Figure 3), but the larger mica particles appear cleaner than the larger illite particles, which are more abundantly coated with finer particles. Bentonite, the smallest of all particles in the study (Table 1), appears relatively larger in the SEM image because the bentonite particles are sensitive enough to moisture in the air that they have clustered together in the SEM image.

3.2. Electrical Sensitivity

Table 1 provides geotechnical material properties of the end-member sediments. For the electrical sensitivity analysis, measured liquid limits with 2 M-brine and kerosene are corrected for the mass of precipitated salt and low specific gravity of kerosene (Jang & Santamarina, 2016, 2017):

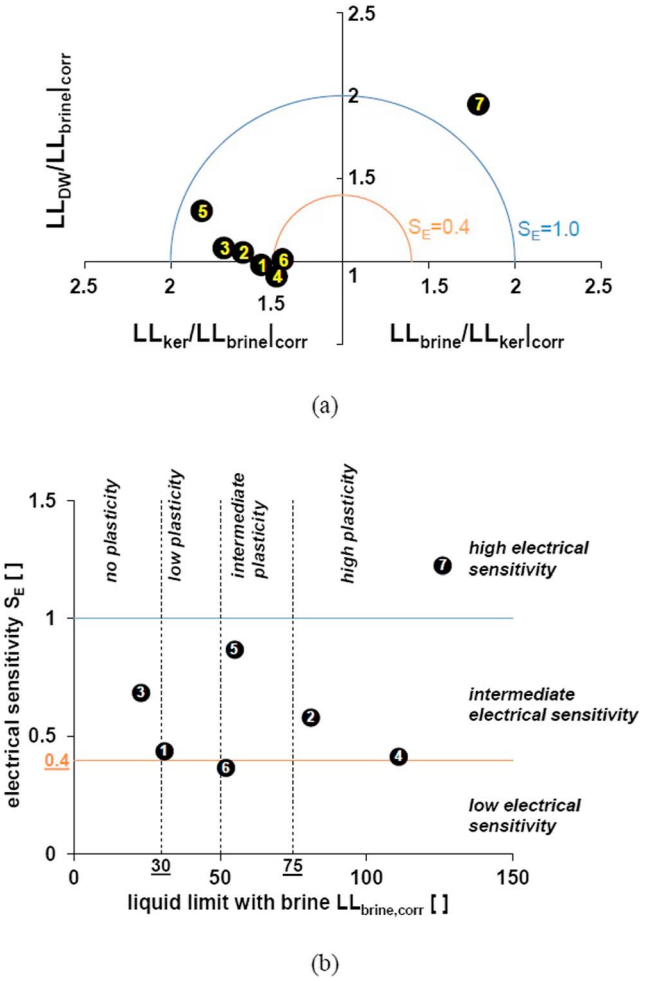

Figure 4. Charts for soil classification based on electrical sensitivity. Numbered black circles refer to the sediments in Table 1. (a) Normalized liquid limit ratio of deionized water and kerosene to brine (refer equations (4) and (5)). (b) Fines classification based on electrical sensitivity, S_E (equation (6)).

$$LL_{brine}|_{corr} = LL_{brine}\frac{1}{1 - c_{brine}\frac{LL_{brine}}{100}}; \tag{2}$$

$$LL_{ker}|_{corr} = \frac{LL_{ker}}{G_{ker}}; \tag{3}$$

$$\left.\frac{LL_{DW}}{LL_{brine}}\right|_{corr} = \frac{LL_{DW}}{LL_{brine}}\left(1 - c_{brine}\frac{LL_{brine}}{100}\right); \tag{4}$$

$$\left.\frac{LL_{ker}}{LL_{brine}}\right|_{corr} = \frac{LL_{ker}}{LL_{brine}}\frac{1 - c_{brine}\frac{LL_{brine}}{100}}{G_{ker}}, \tag{5}$$

where c_{brine} is the NaCl concentration of brine (0.1169 g of NaCl per 1 g of H_2O for the 2 M-brine used here) and G_{ker} is the specific gravity of kerosene, 0.78 (from the manufacturer). The subscripts DW, brine, and ker denote deionized water, brine, and kerosene, respectively. The subscript corr denotes the corrected liquid limit based on the water content rather than the fluid content. Figure 4a presents the corrected ratios from equations (4) and (5) and indicates how those ratios relate to the electrical sensitivity (S_E), which is calculated using equation (6); Jang & Santamarina, 2016, 2017):

$$S_E = \sqrt{\left(\left.\frac{LL_{DW}}{LL_{brine}}\right|_{corr} - 1\right)^2 + \left(\left.\frac{LL_{ker}}{LL_{brine}}\right|_{corr} - 1\right)^2}. \tag{6}$$

Figure 4b presents the soil classification scheme based on electrical sensitivity. Silica silt, $CaCO_3$, diatoms, and mica are considered to have an intermediate electrical sensitivity (Figure 4) because of their sensitivity to electrical permittivity; however, as indicated by similarities between the deionized water and brine liquid limit values in Table 1, these four fines show a smaller sensitivity to ionic concentration, c_0 (brine), than to permittivity, κ' (kerosene). This suggests that DDL-type electrical interactions, which depend on c_0 (equation (1)), are not the dominant controls on the behavior of these fines. Instead, Coulombic attraction due to localized surface charge, which can be accentuated in low-permittivity fluids, develops clustered fabric, which induces higher void ratio than that in water at the liquid limit state.

In contrast, because of its small particle size and high surface charge density, bentonite is strongly influenced by the DDL thickness, which responds to both c_0 and κ' changes in the pore fluid chemistry according to equation (1). Correspondingly, bentonite (HH in Table 1) has the highest electrical sensitivity among the tested fines (Figure 4), with strong sensitivity to changes either in the fluid's ionic concentration (2 M-brine) or permittivity (kerosene). Illite, which like bentonite is a 2:1 clay mineral, has intermediate plasticity but only low electrical sensitivity. The low S_E result may be due to the large grain size (d_{50} = 20 μm, Table 1) of the illite. Illite with smaller grain sizes than was used in this study had an intermediate S_E (Jang & Santamarina, 2016). Kaolin (II in Table 1), a 1:1 clay mineral, shows intermediate plasticity and electrical sensitivity.

The four plasticity ranges shown in Figure 4b are tied to the liquid limit axis, $LL_{brine,corr}$, by the general trend that higher LL_{DW} correlates with higher LL_{brine} and higher PI. Sediments with high plasticity such as clays are expected to show high LL_{DW}, LL_{brine}, and PI, but sometimes, the physical shape of fine particles alters the expected plasticity. For instance, mica (HI in Table 1) and diatoms (HI in Table 1) both have high liquid limits in deionized water and brine. In the case of mica, its platy shape tends to form relatively large interparticle voids (Figure 1e), and diatoms have internal void space in each particle (Figure 3d). The additional void space in the fabric of mica and diatoms allows those sediments to contain additional water, which increases the measured liquid limit (e.g., Tanaka & Locat, 1999). Their plastic limits are elevated for the same reasons,

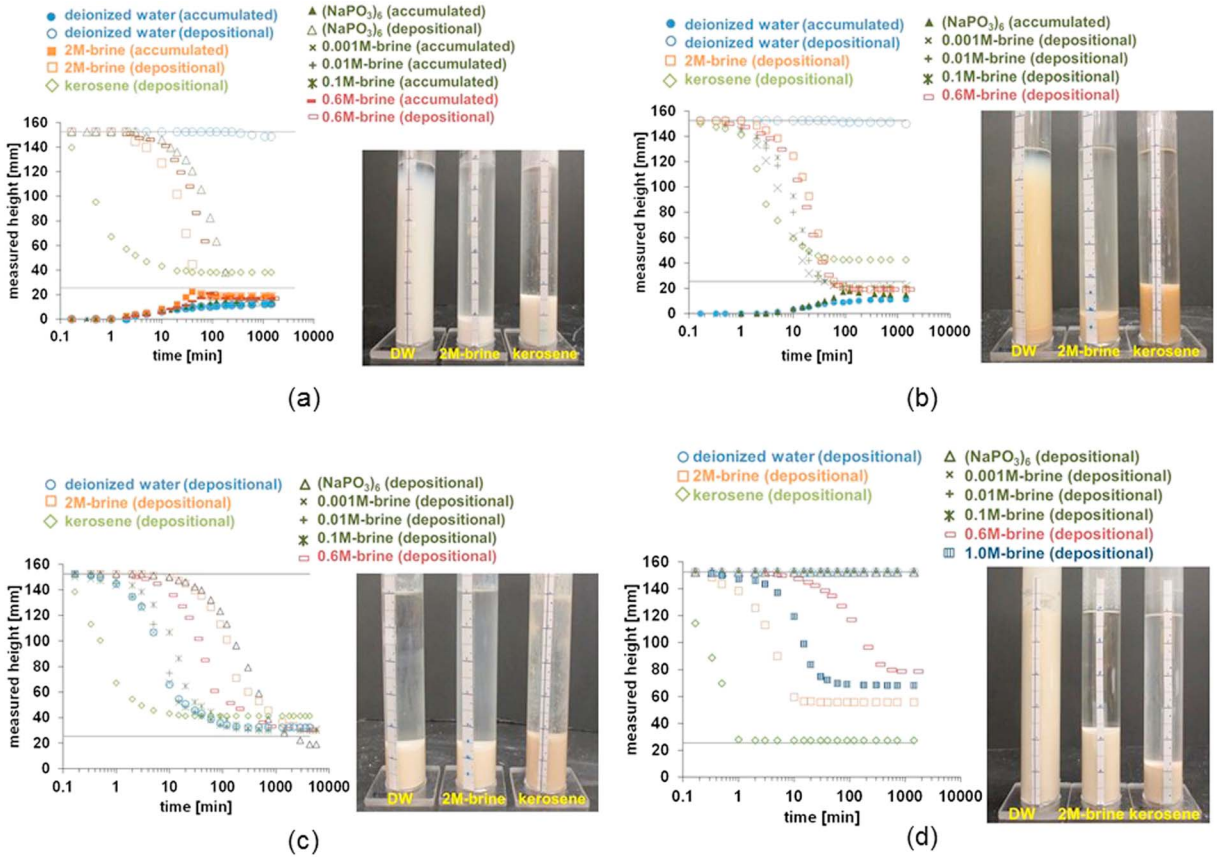

Figure 5. Sedimentation interface heights with time. Horizontal reference lines represent 152.4 mm, the fluid column height, and 25.4 mm, the initial height of each dry, loose-packed specimen. Symbol legends are given in each plot: depositional (open symbols) and accumulated (filled symbols) interface heights refer to the interfaces described in Figure 2. Inset images show examples of each specimen in deionized water, 2 M brine, and kerosene. (a) Silica silt and (b) mica both demonstrate segregated sedimentation. (c) Kaolin and (d) bentonite both demonstrate uniform sedimentation.

however, so their plasticity indices, PI = LL − PL, are actually less than those of the intermediate plasticity fines, such as illite and kaolin (Table 1).

3.3. Sedimentation Tests

The sedimentation test results shown in Figure 5 illustrate several settling trends related to how gravitational force-dominated particles and electrical force-dominated particles interact with pore fluid chemistry to form the sediment fabric (data available online; Jang et al., 2018). These trends can be understood in terms of the general rule that larger particles or particle clusters can gravitationally settle more quickly and with less hindrance from electrical interactions than smaller, individual particles. The magnitude of the pore fluid chemistry effect on clustering and sedimentation is a function of the electrical sensitivity of the sediment. Figure 5 captures distinct sedimentation patterns: segregated and uniform sedimentation. Additional insight is gained from tracking the depositional/accumulated interface height, supernatant turbidity, falling velocity, and final sedimentation height (refer to Figure 2 for term definitions).

3.3.1. Segregated Sedimentation in Aqueous Liquid

Segregated sedimentation occurs in the silica and mica specimens (Figures 5a and 5b), indicating grain size distributions that span two controlling factors for sedimentation. For instance, because of the competition between the gravitational forces and the drag force (Stokes's law), in DW, larger silica particles generally fall more quickly than the smaller silica particles, which remain suspended longer. Silica particles can form DDL, but the DDL is thinner by 3 orders of magnitude relative to the particle diameter for the larger, gravimetrically controlled particles (Dewan et al., 2014) and do not significantly hinder their gravimetric settling rate.

In the silica and mica specimens, larger particles settle to form an accumulated sediment layer at the base of the cylinder increasing the accumulated interface height with time. This accumulated sediment interface can be difficult to distinguish when the suspension above the accumulated interface contains a high enough concentration of the finer particles to become cloudy. The depositional interface can also be difficult to distinguish for specimens with broad grain size ranges because turbidity in these suspensions becomes clear only gradually.

When the ionic concentration of the fluid, c_0, increases, the Sogami-Ise model predicts that the smaller particles can cluster more readily (Figure 1b) and subsequently settle gravimetrically. Thus, the height of the accumulation interface increases as c_0 increases, because a greater fraction of the particles can settle. For example, the accumulation height of silica silt in 2 M brine is higher than that in deionized water (Figure 5a). Also, the depositional interface is more distinct in high c_0 pore fluids because more of the smaller particles become involved in clusters and settle, leaving a less clouded supernatant (cf. Figures 5a and 5b, silica silt below 0.6 M and mica below 0.01 M) .

The dependence of depositional interface clarity on ionic concentration is obvious for mica. As c_0 increases, mica transitions from segregated sedimentation with an accumulation interface and indistinct depositional interface (deionized water, Figure 5b) to uniform sedimentation with a distinct depositional interface and clear supernatant (brine, Figure 5b). The transition occurs at 0.01 M brine. Above this salinity, the smaller mica particles shown in Figure 3b cluster and fall along with the larger mica particles. Settling rate, the speed at which the depositional interface falls, also depends on c_0. This dependence follows one of two distinct trends:

1. With increasing c_0, settlement rate increases for silica silt particles characterized primarily by an overall, relatively uniform, excess surface charge. These particles will form clusters in ion-bearing fluid as suggested by the Sogami-Ise model (Figures 1c and 1d), and the bigger clusters will fall faster.
2. With increasing c_0, settlement rates for platy mica particles characterized by the inhomogeneous distribution of surface charge will decrease. As suggested by the fabric models in Figures 1e and 1f, platy particles with inhomogeneous charge distributions transition from preferentially clustering in an edge-to-face mode (Figure 1e) to a face-to-face mode (Figure 1f). Face-to-face flocculation or clustering occurs more slowly than edge-to-face flocculation slowing the overall clustering and settling process (Palomino & Santamarina, 2005).

3.3.2. Uniform Sedimentation in Aqueous Liquid

Kaolin and bentonite (Figures 5c and 5d) both demonstrate a uniform settlement pattern, showing a clear depositional interface and clear supernatant. Unlike segregated sedimentation, uniform sedimentation indicates that all particles within a specimen are responding to flocculation or clustering processes defined by their electrical interparticle interactions. The clustering process differs from material to material.

Settlement rates for kaolin are controlled by whether the attraction of kaolin particles forms an edge-to-face fabric (Figure 1e) or a face-to-face fabric (Figure 1f). As shown in Figure 1e, kaolin particles in deionized water can flocculate in the edge-to-face fabric. As ionic concentration increases toward the 2 M-brine, kaolin particles begin to form a face-to-face fabric as illustrated in Figure 1f. As described above for mica, face-to-face flocculation is slower than edge-to-face flocculation; hence, the settlement rates decrease with increasing pore water ionic content (Figure 5c).

While the bentonite shows uniform sedimentation (Figure 5d) like kaolin, flocculation of the highly electrically sensitive bentonite (HH in Table 1; Figures 1a and 1b) responds to a different aspect of the particle-fluid interaction than does kaolin. Though bentonite has a platy shape akin to kaolin, its small size and relatively high surface charge density (Meier & Kahr, 1999) promote the formation and effect of a DDL around each particle. In fact, the mixture in deionized water is a paste rather than a suspension because most of the water is bound up in the DDL around each particle. The DDL thickness can be reduced by increasing the c_0 in the fluid (equation (1)), but only after the addition of 0.6 M NaCl (~35 parts per thousand, typical seawater salinity) is the DDL thin enough for the mixture to behave as a fluid-like suspension that allows particles to settle, albeit slowly. Additional increases in c_0 further shrink the DDL thickness, allowing bentonite particles to approach close enough to each other to settle more rapidly.

Unlike silica silt which has similar particle sizes to $CaCO_3$, $CaCO_3$ settles via uniform sedimentation in DW, 2 M-brine, and kerosene, and the supernatant above the depositional height is always clear. This may be

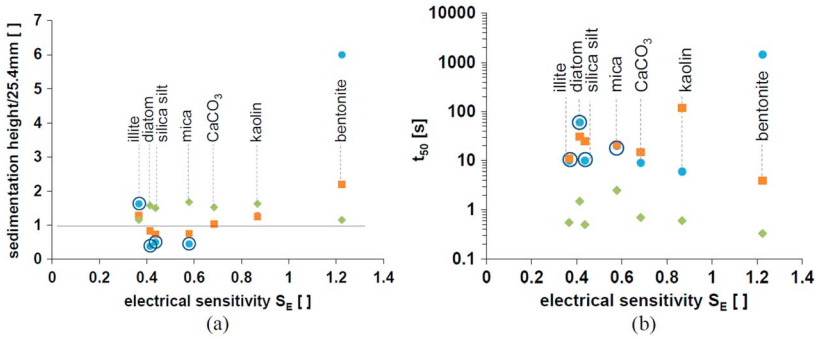

Figure 6. Sedimentation height and falling time in pore fluids of deionized water (solid circle), 2 M-brine (square), and kerosene (diamond) based on the electrical sensitivity of sediments: (a) ratio of final depositional interface height to initial dry height (25.4 mm) and (b) ratio of falling time, t_{50}, when the measurable interface moves half its total travel distance relative to that in 2 M-brine. Because cloudiness obscured the change, if any, in the depositional interface height for silica silt, mica, and diatoms in deionized water (ringed blue circles), the accumulated sediment interface is used instead of the depositional interface.

because $CaCO_3$ has a different chemical composition than silica silt (Stumm, 1992) and generates pronounced clustering in DW compared to silica silt. The falling velocity of depositional interface in DW is similar to that in 2 M-brine, but the falling velocity in kerosene is fastest, as it is for all tested fines. All $CaCO_3$ particles participate in the final accumulated sediment height regardless of fluid. The final heights of $CaCO_3$ in deionized water and brine are close to the 25.4 mm measured for the initial loose sediment in air.

Kerosene allows rapid, uniform sedimentation with a clear supernatant for all the pure fines studied here. The low permittivity of kerosene dramatically reduces DDL thicknesses (equation (1)), and the nonpolar nature of kerosene drives ion precipitation onto particle surfaces (Santamarina et al., 2001; Sposito, 1989), where the ions can create inhomogeneous charge distributions. The combined effects of reduced DDL thickness and inhomogeneous surface charge distributions promote flocculation and rapid sedimentation rates in all tested sediments in kerosene. This generally results in a relatively open, high void ratio sediment fabric illustrated by final sediment heights that exceed those measured in nearly all other fluids. The exceptions are illite and bentonite, which are both 2:1 clay minerals with sedimentation behavior dominated by the DDL thickness. In these two sediments, DDL thickness and, hence, the final sedimentation height both decrease with increasing ionic concentration and are at their minimums in kerosene (see also equation (1)).

3.3.3. Sedimentation With Ion Adsorption Onto Particle Surface

Negative ions in the dispersant, sodium hexametaphosphate $(NaPO_3)_6$, coat the positively charged edges of particles, help the particles disperse, and reduce DDL due to the ionic concentration increase in the fluid (Andreola et al., 2004; Lagaly, 1989). This ion adsorption reduces the edge-to-face attractions in kaolin and mica (Figure 1e). Consequently, the dispersed particles settle relatively slowly, and this is the case for all tested fines. The final height of kaolin and mica in the $(NaPO_3)_6$ solution is less than that in 2 M-brine because the individual particles more densely stack in $(NaPO_3)_6$ than in 2 M-brine. In the case of mica, no data are shown for the depositional interface because the dispersed particles made it impossible to distinguish or track the depositional interface. Though there was no distinguishable depositional interface, the supernatant above the mica's accumulation interface became clearer over time as smaller mica particles were able to cluster and settle in accordance with the Sogami-Ise model (Figure 1d). This is similar to the smaller fines in silica silt, which also form clusters as described in the Sogami-Ise model but do form a discernible depositional interface. Compared to 2 M-brine, the settling rate is slower and the final sedimentation height is less in the dispersant solution.

The fluid ionic concentration also increases in the presence of the dispersant $(NaPO_3)_6$, but the resulting DDL thickness reduction in bentonite is offset by an increase in electrical repulsion as negative ions coat the positive edges of the bentonite and accentuate the electrical repulsion between the negatively charged bentonite particles. This electrical repulsion prevents the bentonite particles from settling within the 4-day duration of the experiment (Figure 5d). A reduction in DDL is inferred because the bentonite/dispersant mixture has enough unbound water to behave like a fluid suspension rather than like the thick paste bentonite forms in deionized water.

3.3.4. Correlations Between Sedimentation and Electrical Sensitivity

Figure 6 shows the relationships between electrical sensitivity and final sediment height (Figure 6a) and between electrical sensitivity and settlement rate (Figure 6b) in the sedimentation tests. These sedimentation height results demonstrate how the void ratio at low effective stress depends on pore water chemistry changes in the tested sediments, a critical issue in determining sediment compressibility. Of the tested sediments, bentonite, having the highest electrical sensitivity, shows the most significant differences in the final settlement height as a function of pore fluid chemistry. For the segregated sedimentation cases (diatoms, silica silt, and mica), a portion of the sediment grains is large enough to be influenced by gravity rather than electrical interactions, so the overall measured electrical sensitivity is low. Sedimentation height differences between deionized water and the other fluids appear accentuated for segregated sedimentation because most fines in deionized water remain suspended in the supernatant during sedimentation, so only a fraction of fines contributes to the final measured sediment height, except in the low-permittivity kerosene case.

Differences in sedimentation behavior due to electrical sensitivity are also observed when measuring settlement rates. As noted previously, kerosene causes fast settlement in all cases. Based on ionic concentration trends shown in Figure 5, the Figure 6b rate results show sedimentation rate increases for silica silt and bentonite but decreases in mica and kaolin with increasing ionic concentration. As shown in Figure 6b, a high electrical sensitivity index value indicates that sediments will settle at dramatically different rates when pore water salinity changes. In the field, predicting whether the settlement rate increase or decreases requires knowing the mineralogy. Knowing which fines are present indicates which of the electrical interaction mechanisms shown in Figure 1 exerts the primary control on the fines involved.

The apparent impact of ionic concentration on sedimentation rate is muted in Figure 6b for the sediments with low electrical sensitivity, in part because of the segregated sedimentation in illite, diatoms, silica silt, and mica. Because of the relatively broad particle size ranges in these sediments, the suspended sediment does not form a distinct depositional interface, so Figure 6b plots the movement of the accumulated sediment interface for these sediments. The impact of salinity change in these sediments can be seen more obviously in the evolution of turbidity, which was assessed qualitatively by eye. The turbidity due to smaller particles in the supernatant above the depositional interface decreases more quickly with increasing ionic concentration. The supernatant above the depositional interface also becomes clearer more quickly as the ionic concentration increases. The improvement in supernatant clarity is due to the presence of pore water ions, which help more particles cluster and settle below the depositional interface.

3.4. Consolidation Tests

Figure 7 shows how the consolidation results for silica silt, mica, kaolin, and bentonite depend on pore fluid chemistry (data available online; Jang et al., 2018). The compression indices derived from consolidation tests represent the change in void ratio due to effective stress changes. The compression index, C_c (Figure 8a), and recompression index, C_r (Figure 8b), are calculated from the slope of the compression curve during the initial compression and during recompression, respectively, from equation (7) below and are presented in Table 2:

$$C_c \text{ or } C_r = \frac{e_{100\text{kPa}} - e_{1{,}000\text{kPa}}}{\log_{10}\left(\frac{1{,}000\text{kPa}}{100\text{kPa}}\right)} = e_{100\text{kPa}} - e_{1{,}000\text{kPa}} \tag{7}$$

where $e_{100\text{kPa}}$ and $e_{1000\text{kPa}}$ are the void ratios at 100 kPa and at 1,000 kPa vertical effective stress, respectively.

Sediment with a higher void ratio fabric will generally have a higher final sedimentation height (section 3.3) and a higher compressibility (Burland, 1990; Cerato & Lutenegger, 2004; Hong et al., 2010; Sridharan & Nagaraj, 2000; Tiwari & Ajmera, 2011). The fabric can be altered by changes in the pore fluid chemistry, which in turn affects the void ratio. The dependence of sediment fabric on pore fluid chemistry is captured in the sediment's electrical sensitivity and observed in the sedimentation behavior, so the measured electrical sensitivities (Figure 4b) and final sedimentation height results (Figure 6a) are used here to provide insight into the observed compressibility trends.

Segregated sedimentation results are relevant to the compression index behavior for silica silt, mica, and diatoms. In deionized water, the finer particles that remain in suspension (Figures 2b, 5a, and 5b) can remain in the pore fluid in the compression test specimen, floating in the free pore space without interacting with the

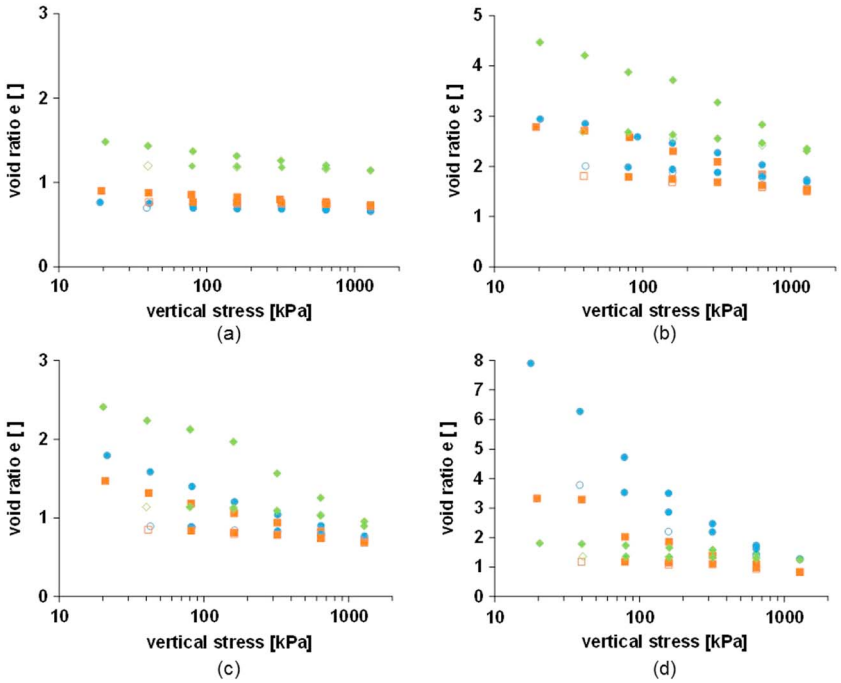

Figure 7. Consolidation results in deionized water (circle), 2 M brine (square), and kerosene (diamond) for (a) silica silt, (b) mica, (c) kaolin, and (d) bentonite. Solid symbols are loading and reloading steps, and the open symbols are unloading steps.

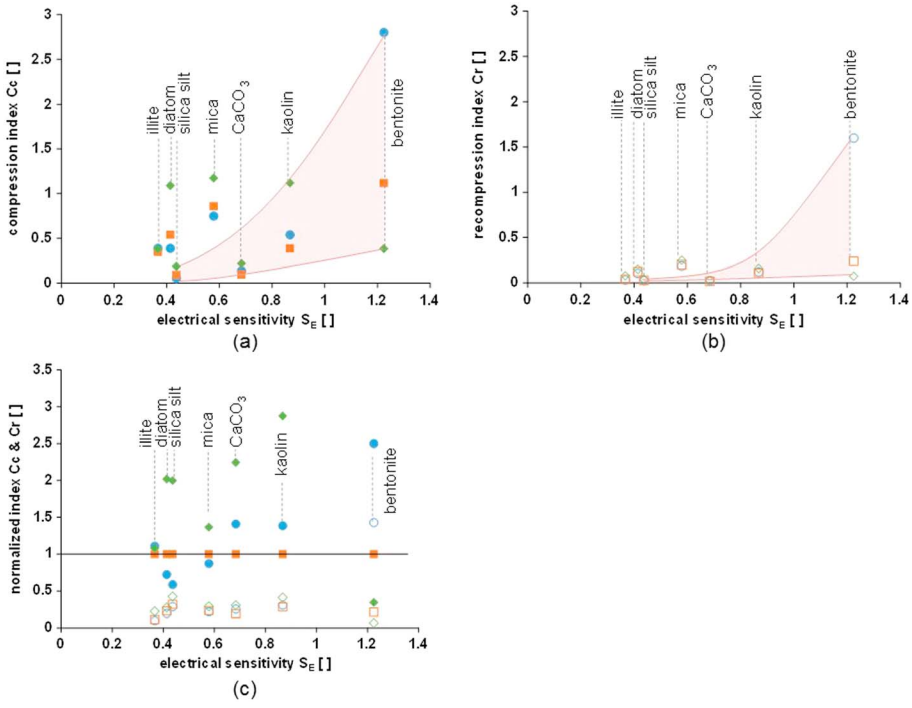

Figure 8. Dependence of the (a) compression (solid symbols) and (b) recompression indices (open symbols) on electrical sensitivity and (c) results normalized to C_c and C_r of each sediment in 2 M-brine. The shaded area in (a) and (b) represents possible ranges of the compression and recompression index as a function of electrical sensitivity after removing sediments that have unusually high void ratios due to their physical shapes. Symbol shape definitions are the same as in Figure 7.

Table 2
Compression and Recompression Indices of End-Member Sediments

		Compression index C_c			Recompression index C_r		
No.	Sediments	Deionized water	2 M brine	Kerosene	Deionized water	2 M brine	Kerosene
1	silica silt	0.055	0.094	0.188	0.027	0.03	0.04
2	mica	0.74	0.86	1.174	0.187	0.20	0.25
3	$CaCO_3$	0.138	0.098	0.22	0.025	0.019	0.03
4	diatom	0.39	0.54	1.09	0.106	0.124	0.149
5	kaolin	0.5*	0.39*	1.12	0.11*	0.11*	0.16
6	illite	0.39*	0.352*	0.38	0.06*	0.04*	0.079
7	bentonite	2.8*	1.12	0.385	1.61	0.24	0.075

Note. Height of the oedometer rigid ring is 19.05 mm. Where noted by *, the ring height is 25.4 mm.

larger particles (Figure 9a). When the pore fluid is 2 M-brine or kerosene, however, finer particles would settle along with the larger particles, coexisting at contacts between large grains and elsewhere in the pore space (Figure 9d). Thus, void ratio and compressibility in 2 M-brine and kerosene increase as additional fines collect at larger-particle contacts and participate in bearing the applied stress on the sediment (Figure 9d).

In kaolin, platy particles demonstrating uniform sedimentation, the compressibility is higher when the specimen has the high void ratio, edge-to-face fabric observed in deionized water or kerosene (Figure 1e), and lower compressibility when the specimen has the low void ratio face-to-face fabric (Figure 1f) observed in brine. In the case of the highly electrically sensitive bentonite, the void ratio, and hence compressibility, scales with DDL thickness (Figure 9b). Thus, void ratio and compressibility increase with decreasing ionic concentration in the pore water equation (1).

Illite, diatoms, and mica fall outside the shaded region in Figure 8a, showing high compressibility that reflects more on their particle morphology than their low electrical sensitivity: illite and mica are platy particles, but they are able to form high-compressibility, high void ratio, edge-to-face fabrics (Figure 1e), even at salinities that would cause the more electrically sensitive platy kaolin to form low compressibility, low void ratio, face-to-face fabrics (Figures 1f and 8a). Diatoms, because they are often broken into angular, irregular shards (Figure 3d) and have internal porosity, are also able to form relatively high void ratio fabrics regardless of the pore fluid.

To examine the dependence of compressibility on electrical sensitivity rather than physical morphology, compression index can be normalized to the compression index for the 2 M-brine for each sediment and pore fluid (Figure 8c). The general trend of $C_{c,DW} < C_{c,brine}$ in sediments with low electrical sensitivity (silica silt and diatoms) captures the sediment-stiffening effects of fines segregating away from coarse-grained contacts during sedimentation. This ordering highlights how microscale grain distribution behaviors suggested by the sedimentation tests—in this case the distribution of smaller and larger particles at grain contacts (Figures 9a and 9d)—can be inferred to occur even in saturated, remolded specimens formed by physically mixing sediment and fluid rather than by allowing the particles to collect via deposition.

Kerosene generally yields high void ratio sediment fabrics that manifest themselves as the most compressible particle arrangement in this study. The exceptions are bentonite and illite. Bentonite, with its high electrical sensitivity, settles into its densest fabric in the presence of kerosene because of the minimized DDL thickness. Like bentonite, illite is a 2:1 clay mineral and should respond to pore fluid changes in a similar manner. Though the DDL thickness for illite also decreases in brine and kerosene, similar to the pattern of bentonite (Figure 6a), the compression index of illite is essentially independent of pore fluid chemistry due to size effect as described in section 3.2 and also observed by Meade (1964).

Recompression indices for the tested sediments are approximately a quarter to a half of the brine compression index, $C_{c,brine}$ (Figure 8c). The tested recompression indices are uniformly low with negligible dependence on pore fluid chemistry except for the highly electrically sensitive bentonite. The recompression index behavior is due to the virgin vertical stress destroying the initial fabric to the point at which electrical forces are not strong enough to recreate higher void ratio fabrics during unloading (e.g., Figure 9c). However, because the DDL develops regardless of the fabric and transfer stress (Figure 9b), bentonite in deionized

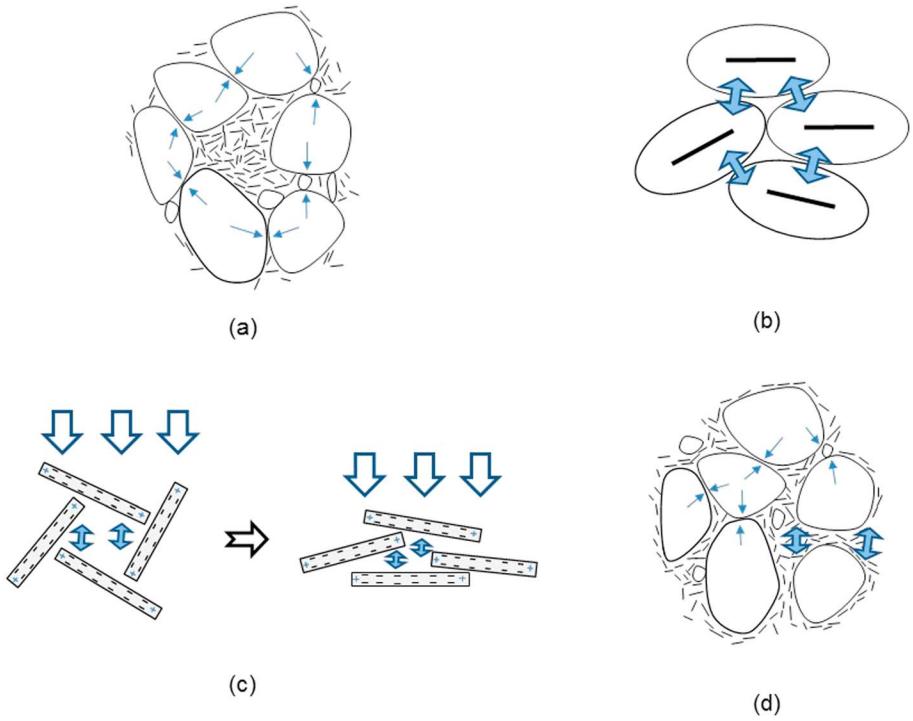

Figure 9. Fabric-based external stress transfer mechanisms. Larger grains are shown as irregular outlined shapes; electrically sensitive clays are shown as dashes. (a) Skeletal force-dominated fabric, which can form during segregated sedimentation, experiences stress transfer (blue arrows) primarily through contacts between large grains such as silica silt in deionized water. (b) Electrical force-dominated fabric such as the bentonite (dashes) is controlled by DDL thickness (ellipsoids) and thus tends to be relatively compressible. (c) Electrical force-dominated fabric, such as kaolinite, can form high void fabric at low stress, but that fabric is compressible and will collapse under moderate stress. (d) Mixed fabric of skeletal (single-ended arrows) and electrical stress-transfer contacts (double-ended arrows) such as silica silt in 2 M-brine (Hueckel, 1992; Mitchell & Soga, 2005; Santamarina et al., 2001).

water reforms or swells to higher void ratios, a typical characteristic of swelling clays that generates a high recompression index compared to what develops in brine or kerosene, which generate only a thin DDL.

4. Implications for Gas Hydrate-Bearing Sediments

Gas hydrate is a crystalline compound in which water molecules encage individual gas molecules (Sloan & Koh, 2008). Gas hydrate, primarily methane gas hydrate, exists in the sediments of marine continental slope and permafrost environments around the world (Kvenvolden, 1988; Ruppel & Kessler, 2017), and production tests have shown that methane can be extracted from gas hydrates filling the pore space of sands in permafrost (Uddin et al., 2012) and marine sediments (Yamamoto et al., 2014). Field tests in permafrost (Collett et al., 2009) and marine environments (Yamamoto et al., 2017), and reservoir modeling results (Kurihara, Funatsu, et al., 2011; Moridis & Reagan, 2007a, 2007b), indicate that depressurizing the sediment pore space is the most effective approach for destabilizing the gas hydrate and liberating the methane for production.

During depressurization, the sediment formation experiences a vertical effective stress increase due to the pore pressure reduction and will also experience pore fluid freshening due to the fresh water released from dissociating gas hydrate. When a unit volume of gas hydrate breaks down to release methane, 0.79 units of fresh water are also released (Sloan & Koh, 2007), bathing formerly brine-saturated pore spaces in fresh water (Hesse & Harrison, 1981). For a given sediment pore, and assuming an initial gas hydrate saturation within a 60–70% range observed in marine and permafrost environments (Kurihara, Sato, et al., 2011; Fujii et al., 2015), gas hydrate dissociation would reduce the salinity to 35–45% of original value. Continued depressurization and dissociation prevents pore fluid from reequilibrating to its original salinity, so fines that had previously been in a high ionic concentration, brine environment will respond to the depressurization according to their behaviors in low ionic concentration fluids.

Since fines are still present within and adjacent to gas hydrate-bearing sands (Egawa et al., 2015; Hyodo et al., 2017; Ripmeester et al., 2005; Winters et al., 2011), this study offers insights into how the behavior of fines can modify the sediment formation response to depressurization, particularly near the production well where the compaction of sediment that no longer hosts hydrate can reduce permeability and potentially limit reservoir production efficiency. Three responses to pore water freshening in hydrate-bearing sediment are considered here: changing in situ compressibility, fines migration, and the physical property alterations expected for naturally occurring hydrate-bearing sediment recovered in pressure cores.

4.1. Compressibility

Compressibility depends on sediment fabric, which transfers applied vertical stress (Figure 9). Since even a coarse-grained hydrate-bearing reservoir can contain fines, the reservoir fabric could be a skeletal force-dominated fabric with coarser grains in contact with each other (Figure 9a) or a mixed fabric with fines existing between some of the coarse grains (Figure 9d). The sedimentation results (section 3.3) suggest that the saline marine sediment would be conducive for developing a mixed fabric because ions in fluid would assist clustering in fines and promote more homogeneous sedimentation.

As these predominantly coarse-grained sediments are buried, hydrate has a chance to grow in the available pore space. Naturally occurring hydrate formation is slow, requiring on the order of 10^5 years for hydrate reservoirs to form from the methane dissolved in upwelling pore fluid (Xu & Ruppel, 1999; Zatsepina & Buffett, 1997). Consequently, the salt excluded from the pore water as hydrate forms has time to diffuse away, and the pore water salinity can be considered constant (Xu & Ruppel, 1999).

As hydrate dissociates relatively rapidly due to the imposed depressurization during production activities, however, the pore water freshens. Figures 7c, 7d, 8a, and 8c suggest that fines will respond to the freshened pore fluid and transition to larger void ratio, more compressible fabrics, particularly if those fines are predominantly the more electrically sensitive fines such as smectite (e.g., montmorillonite, which is the primarily mineral of the bentonite tested in this work) or kaolinite, both of which are known to occur in the gas hydrate-bearing sands in the Nankai Trough (Egawa et al., 2015; Hyodo et al., 2017). As pore fluid chemistry is affecting the fines in the sediment fabric, the depressurization-induced effective stress increase can lead the sediment back onto a virgin compression curve (Santamarina et al., 2015). Since pore fluid chemistry effects on high electrical sensitivity fines such as montmorillonite tend to diminish for the mechanical stresses above 5 MPa (Meade, 1964; Olson & Mesri, 1970), the sediment compressibility will be responding to a complex competition between mechanical stress and physicochemical stress.

A second compressibility consideration concerns the behavior of thin, fine-grained, low hydrate saturation interbeds between the coarser, gas highly hydrate-saturated reservoir layers. At Green Canyon Site 995, in the Gulf of Mexico, for example, these interbeds are 20–30 cm thick (Boswell et al., 2012) and can react to pore water freshening in the adjacent sandy gas hydrate layers. The leaching of in situ brine with increasing vertical stress could be analogous to sensitive clays on land (Bjerrum, 1967; Crawford, 1968; Skempton & Northey, 1953) if the seal sediment consists of clay minerals that are also high-plasticity fine grains with high/intermediate electrical sensitivity.

4.2. Fines Migration

Production tests at the Mallik permafrost test site (Uddin et al., 2012) and the Nankai marine test site (Yamamoto et al., 2014) were both terminated due to the intrusion of sand into the production well from the hydrate-bearing reservoir sand layer. As the in situ fluid flow rates required to move sand into the borehole are approximately an order of magnitude higher than those required to detach and mobilize fines (Oyama et al., 2016), pore water freshening can make certain fines, such as kaolinite, more prone to detachment and mobilization (Mohan et al., 1993).

Two potential consequences of fines migration are permeability reduction and weakening of the coarse-grained sediment. Fines migration can lead to reduced permeability via pore-throat clogging, particularly near the production well where mobilized fines become more concentrated by the inward radial pore fluid flow (Valdes & Santamarina, 2007). As fines detach from coarser grains, particularly from the contacts between coarser grains in a mixed fabric (Figure 9d), the detachment can disturb effective stress chains in the mixed fabric and weaken the sediment shear strength. A reduction in the shear strength facilitates detachment of the coarser grains themselves (Uchida et al., 2017), so that the sand particles can be

entrained in multiphase flow toward the production well. When a sandy reservoir is destructured during depressurization-induced dissociation process, sand production can occur (Yamamoto et al., 2014).

4.3. Physical Property Alterations in Pressure Cores

Because gas hydrates are only stable in proper pressure and temperature within the gas hydrate stability boundary, recovering natural gas hydrate-bearing sediment suitable for physical property testing must be done using pressure cores, which retain near-in situ pressures throughout the core's recovery process and measurement process (Priest et al., 2015; Santamarina et al., 2015; Schultheiss et al., 2011; Yoneda et al., 2015, 2017; see also Dai et al., 2017, for a recent review of pressure coring and measurement technology). Pressure cores are generally stored with pressurized fresh water in contact with the sediment, and due to the complexities and logistics required to set up pressure core measurements in the laboratory, cores can remain in storage for months or more prior to testing. During storage of short samples (6 to 17 cm) intended for experiments near in situ pressure, the core's in situ saline pore fluid can be freshened by the surrounding pressure-chamber water used for maintaining nearly in situ pressures. Based on the simplified 1-D diffusion equation ($t = L^2/D$, where the t is diffusion time, L diffusion distance, and D diffusion coefficient), the minimum time for the core's average pore water salinity to fall to half its original value a distance L = 25.4 mm (1 in.) from the core end is approximately 5 days when $D = 1.5 \times 10^{-9}$ m^2/s (Vitagliano & Lyons, 1956). Even without net flow through the core during storage, the pore fluid exchange could be expedited by ambient cyclic fluctuations such as temperature change and vibration (Cowin, 1999; Piekarski & Munro, 1977; Wang et al., 2000). Caution should be applied when analyzing such cores, with the understanding that macroscopic properties of stored cores (e.g., compressibility) may reflect values associated with freshened pore water rather than the in situ saline pore water.

5. Conclusions

This work demonstrates how the liquid limit-based electrical sensitivity can be used to anticipate complex sedimentation and compressibility behavior from a knowledge of the sediment mineralogy. Electrical sensitivity captures how changes in pore water chemistry alter microscale (interparticle) interactions, and these interactions manifest themselves as alterations of macroscopic properties such as sediment compressibility. Inherently, high electrical sensitivity sediment transforms its fabric due to pore fluid chemistry changes with the sedimentation pattern and compression behavior shifting accordingly. Though the results presented here are measured on pure, end-member fines, the nearly universal presence of fines in sediment means that the results are important even when interpreting the response of primarily coarse-grained sediments to evolving stress or pore fluid conditions. Based on electrical sensitivity links with fundamental geotechnical property measurements such as particle sizes and particle shapes, the impact of pore fluid chemistry changes on sediment properties can be predicted through the following generalizations:

1. Stress transfer in the gravitational force dominated fabric or low electrical sensitivity fines fabric is primarily across contacts between the larger grains, so volume changes during consolidation are mainly due to the mechanical behavior of particles at contacts between larger grains.
2. During sedimentation, electrically sensitive fines show visual differences in settling rate and final sedimentation height. Due to particle shape and surface charge distribution, the fabrics and stress transfer mechanisms of fines with intermediate and high electrical sensitivity are controlled by electrical force-dominated fabric mechanisms: DDL (e.g., bentonite), edge-to-face fabric and face-to-face fabric (e.g., kaolin), and the Sogami-Ise model of attraction (e.g., suspended silica particles).
3. Although the electrical sensitivity index does not indicate the mechanisms by which electrical interactions and particle shapes determine sediment fabric, the electrical sensitivity of sediments provides insights to changes in the compressibility in a given sediment to ionic concentration and permittivity changes in pore fluid chemistry.
4. During depressurization to extract methane from gas hydrate, the electrical sensitivity index provides insight into sediment fabric and compressibility changes due to freshening. The extent to which fines enhance or mitigate sediment compression depends on the specific types and concentration of fines in the system. However, the combination of pore water freshening and fluid flow is anticipated to increase the capacity of fines to mobilize and subsequently reduce permeability via pore-throat clogging and also to disturb coarse-grained sediment contact and exacerbate sand production.

Appendix A

The Poisson-Boltzmann equation for charge and potential distribution (Israelachvili, 2011; Santamarina et al., 2001):

$$\frac{\partial^2\psi(x)}{\partial x^2} = \frac{2c_0z^2F^2}{\varepsilon_0\varepsilon' RT}\psi(x), \tag{A1}$$

where ψ (x) is the electrical potential at distance x from surface, c_0 is bulk fluid concentration, z is ion valence, F is Faraday's constant 9.6485 × 10^4C/mol, ε_0 is the permittivity of free space 8.85 × 10^{-12}F/m, ε' is relative permittivity, R is the gas constant 8.314 J/(K/mol), and T is temperature.

Diffuse double-layer thickness ϑ:

$$\vartheta = \frac{1}{\kappa} = \sqrt{\frac{\varepsilon_0 R}{2F^2}\frac{\kappa' T}{c_0 z^2}} = \sqrt{\frac{\varepsilon_0 k_B}{2e_0^2 N_{av}}\frac{\varepsilon' T}{c_0 z^2}}, \tag{A2}$$

where k_B is Boltzmann's constant 1.38 × 10^{-23} J/K, e_0 is the electron charge 1.602 × 10^{-19}C, and N_{av} is Avogadro's number 6.022 × 10^{23} mol^{-1}. Diffuse double-layer repulsion R_{DL} (Pa):

$$R_{DL} = 64RTc_0e^{-\frac{r}{\vartheta}}, \tag{A3}$$

where the r is distance between two surfaces. Van der Waals interaction A_{vdw} (Pa) between two flat surfaces:

$$A_{vdw} = -\frac{A_h}{6\pi r^3}, \tag{A4}$$

where A_h (J) is Hamaker constant.

The Poisson-Boltzmann equation for the total electrostatic energy of the system in Sogami-Ise model (Sogami, 1983; Sogami & Ise, 1984):

$$\varepsilon\left(\nabla^2 - \kappa^2\right)\psi(x) = -4\Sigma_{n=1}^{N} Z_n e_0 \rho_n(x) - 4\pi \sum_{i=1}^{v} n_{i0} z_i e_0, s \tag{A5}$$

where ε is the permittivity, v is the number of species of simple ions, n_{i0} is the average number of ions of type i per unit volume, ρ_n (x) is the charge distribution function for macromolecule (radius = a) with electric charge Ze_0 in terms of R_l the center of gravity

$$\rho_n(x) = \frac{\delta(|x - R_l| - a)}{4\pi a^2}, \tag{A6}$$

and ψ (x) potential field is

$$\psi(x) = \phi(x) + \frac{4\pi e}{\epsilon\kappa^2}\Sigma_i n_{i0} z_i, \tag{A7}$$

where the ϕ (x) is shifted potential field. The total electrostatic energy of the system is

$$E = \frac{\varepsilon}{8\pi}\int[\nabla\psi(x)]^2 dx = \frac{1}{2}\int\nabla\psi(x)\left[-\frac{\varepsilon\kappa^2}{4\pi}\phi(x)\right]dV + \frac{1}{2}\Sigma_n Z_n e_0 \int\psi(x)\rho_n(x)dx. \tag{A8}$$

The first term on the right-hand side entails the attractive force for particle clustering.

Acknowledgments
This work was supported by the U.S. Geological Survey's Gas Hydrates Project, by an interagency agreement between the U.S. Geological Survey and the Department of Energy (DE-FE00-26166), and by a Department of Energy grant awarded to Louisiana State University (DE-FE00-28966). The authors wish to thank L-G. Boze for his apparatus construction and laboratory measurements. This report was prepared as an account of work sponsored by an agency of the United States Government. Any use of trade, firm, or product name is for descriptive purposes only and does not imply endorsement by the U.S. Government. The authors wish to thank C. Ruppel (USGS) for constructive comments on the manuscript. The experimental data are available online in the USGS science database (http://doi.org/10.5066/F77M076K; see Jang et al., 2018, in the reference list).

References

Anderson, B., Boswell, R., Collett, T. S., Farrell, H., Ohtsuki, S., White, M. & Zyrianova, M. (2014). Review of the findings of the Ignik Sikumi CO_2-CH_4 gas hydrate exchange field trial. *Proceedings of the 8th International Conference on Gas Hydrates,* United States: China Geological Survey, Beijing, China.

Andersson-Skold, Y., Torrance, J. K., Lind, B., Oden, K., Stevens, R. L., & Rankka, K. (2005). Quick clay—A case study of chemical perspective in Southwest Sweden. *Engineering Geology*, *82*(2), 107–118. https://doi.org/10.1016/j.enggeo.2005.09.014

Andreola, F., Castellini, E., Manfredini, T., & Romagnoli, M. (2004). The role of sodium hexametaphosphate in the dissolution process of kaolinite and kaolin. *Journal of the European Ceramic Society*, *24*(7), 2113–2124. https://doi.org/10.1016/S0955-2219(03)00366-2

Arnott, R. (1965). Particle sizes of clay minerals by small-angle X-ray scattering. *The American Mineralogist*, *50*, 1563–1575.

ASTM (2000). Standard test methods for minimum index density and unit weight of the soil and calculation of relative density. ASTM D4254. West Conshohocken, PA.

ASTM (2005). Standard test methods for liquid limit, plastic limit, and plasticity index of the soil ASTM D4318. West Conshohocken, PA.

ASTM (2007). Standard test method for particle-size analysis of the soil ASTM D422. West Conshohocken, PA.

ASTM (2011a). Standard practice for classification of the soil for engineering purposes (Unified Soil Classification System). ASTM D2487. West Conshohocken, PA.

ASTM (2011b). Standard test methods for one-dimensional consolidation properties of the soil using incremental loading. ASTM D2435. West Conshohocken, PA.

Austad, T., Strand, S., Madland, M. V., Puntervold, T., & Korsnes, R. I. (2008). Seawater in chalk: An EOR and compaction fluid. *SPE Reservoir Evaluation & Engineering*, *11*(04), 648–654. https://doi.org/10.2118/118431-PA

Bahk, J. J., Kim, D. H., Chun, J. H., Son, B. K., Kim, J. H., Ryu, B. J., et al. (2013). Gas hydrate occurrences and their relation to host sediment properties: Results from second ulleung basin gas hydrate drilling expedition, East Sea. *Marine and Petroleum Geology*, *47*, 21–29. https://doi.org/10.1016/j.marpetgeo.2013.05.006

Bandini, P., & Sathiskumar, S. (2009). Effects of silt content and void ratio on the saturated hydraulic conductivity and compressibility of sand-silt mixtures. *Journal of Geotechnical and Geoenvironmental Engineering*, *135*(12), 1976–1980. https://doi.org/10.1061/(ASCE)GT.1943-5606.0000177

Bennett, R. H., Fischer, K. M., Lavoie, D. L., Bryant, W. R., & Rezak, R. (1989). Porometry and fabric of marine clay and carbonate sediments—Determinants of permeability. *Marine Geology*, *89*(1–2), 127–152. https://doi.org/10.1016/0025-3227(89)90030-3

Bennett, R. H., & Hulbert, M. H. (1986). Clay microstructure. International Human Resources Development Corporation, Boston, MA.

Bjerrum, L. (1967). Engineering geology of Norwegian normally-consolidated marine clays as related to settlements of buildings. *Geotechnique*, *17*(2), 83–118. https://doi.org/10.1680/geot.1967.17.2.83

Bolt, G. H. (1956). Physico-chemical analysis of the compressibility of pure clays. *Geotechnique*, *6*(2), 86–93. https://doi.org/10.1680/geot.1956.6.2.86

Boswell, R., Collett, T. S., Frye, M., Shedd, W., McConnell, D. R., & Shelander, D. (2012). Subsurface gas hydrates in the northern Gulf of Mexico. *Marine and Petroleum Geology*, *34*(1), 4–30. https://doi.org/10.1016/j.marpetgeo.2011.10.003

British Standard Institute BSI (1990). Methods of test for soils for civil engineering purpose. BS 1377. London.

Burland, J. B. (1990). 30th Rankine lecture—On the compressibility and shear-strength of natural clays. *Geotechnique*, *40*(3), 329–378. https://doi.org/10.1680/geot.1990.40.3.329

Carraro, J. A. H., Prezzi, M., & Salgado, R. (2009). Shear strength and stiffness of sands containing plastic or nonplastic fines. *Journal of Geotechnical and Geoenvironmental Engineering*, *135*(9), 1167–1178. https://doi.org/10.1061/(ASCE)1090-0241(2009)135:9(1167)

Carrier, W. D., & Beckman, J. F. (1984). Correlations between index tests and the properties of remoulded clays. *Geotechnique*, *34*(2), 211–228. https://doi.org/10.1680/geot.1984.34.2.211

Cerato, A. B., & Lutenegger, A. J. (2004). Determining intrinsic compressibility of fine-grained soils. *Journal of Geotechnical and Geoenvironmental Engineering*, *130*(8), 872–877. https://doi.org/10.1061/(ASCE)1090-0241(2004)130:8(872)

Chen, J., Anandarajah, A., & Inyang, H. (2000). Pore fluid properties and compressibility of kaolinite. *Journal of Geotechnical and Geoenvironmental Engineering*, *126*(9), 798–807. https://doi.org/10.1061/(ASCE)1090-0241(2000)126:9(798)

Collett, T. S., Johnson, A. H., Knapp, C. C., & Boswell, R. (2009). Natural gas hydrates: A review. In T. S. Collett, A. H. Johnson, C. C. Knapp, & R. Boswell (Eds.), *Natural gas hydrates—Energy resource potential and associated geologic hazards*, *AAPG Memoir* (Vol. 89, pp. 146–219). Tulsa, OK: American Association of Petroleum Geologists (AAPG).

Cowin, S. C. (1999). Bone poroelasticity. *Journal of Biomechanics*, *32*(3), 217–238. https://doi.org/10.1016/S0021-9290(98)00161-4

Crawford, C. B. (1968). Quick clays of eastern Canada. *Engineering Geology*, *2*(4), 239–265. https://doi.org/10.1016/0013-7952(68)90002-1

Dai, S., Boswell, R., Waite, F. W., Jang, J., Lee, J. Y., & Seol, Y. (2017). What has been learned from pressure cores. *The 9th International Conference on Gas Hydrates*, Denver, Colorado, USA, June 25–30, 2017.

Derjaguin, B., & Landau, L. (1941). Theory of the stability of strongly charged lyophobic sols and of the adhesion of strongly charged particles in solutions of electrolytes. *Acta Physicochimica U.R.S.S.*, *15*(6), 633–662.

Dewan, S., Carnevale, V., Bankura, A., Eftekhari-Bafrooei, A., Fiorin, G., Klein, M. L., & Borguet, E. (2014). Structure of water at charged interfaces: A molecular dynamics study. *Langmuir*, *30*(27), 8056–8065. https://doi.org/10.1021/la5011055

Di Maio, C., & Fenelli, G. B. (1994). Residual strength of kaolin and bentonite: The influence of their constituent pore fluid. *Geotechnique*, *44*(2), 217–226. https://doi.org/10.1680/geot.1994.44.2.217

Egawa, K., Nishimura, O., Izumi, S., Fukami, E., Jin, Y., Kida, M., et al. (2015). Bulk sediment mineralogy of gas hydrate reservoir at the East Nankai offshore production test site. *Marine and Petroleum Geology*, *66*, 379–387. https://doi.org/10.1016/j.marpetgeo.2015.02.039

Fernandez, F., & Quigley, R. M. (1985). Hydraulic conductivity of natural clays permeated with simple liquid hydrocarbons. *Canadian Geotechnical Journal*, *22*(2), 205–214. https://doi.org/10.1139/t85-028

Frederick, J. M., & Buffett, B. A. (2015). Effects of submarine groundwater discharge on the present-day extent of relict submarine permafrost and gas hydrate stability on the Beaufort Sea continental shelf. *Journal of Geophysical Research: Earth Surface*, *120*, 417–432. https://doi.org/10.1002/2014JF003349

Fujii, T., Suzuki, K., Takayama, T., Tamaki, M., Komatsu, Y., Konno, Y., et al. (2015). Geological setting and characterization of a methane hydrate reservoir distributed at the first offshore production test site on the Daini-Atsumi Knoll in the eastern Nankai Trough, Japan. *Marine and Petroleum Geology*, *66*, 310–322.

Glass, R. J., Conrad, S. H., & Peplinski, W. (2000). Gravity-destabilized nonwetting phase invasion in macroheterogeneous porous media: Experimental observations of invasion dynamics and scale analysis. *Water Resources Research*, *36*, 3121–3137. https://doi.org/10.1029/2000WR900152

Hesse, R., & Harrison, W. E. (1981). Gas hydrates (clathrates) causing pore-water freshening and oxygen isotope fractionation in deep-water sedimentary sections of terrigenous continental margins. *Earth and Planetary Science Letters*, *55*(3), 453–462. https://doi.org/10.1016/0012-821X(81)90172-2

Holtz, R. D., Kovacs, W. D., & Sheahan, T. C. (2011). *An introduction to geotechnical engineering*. Upper Saddle River, NJ: Prentice Hall.

Hong, Z. S., Yin, J., & Cui, Y. J. (2010). Compression behaviour of reconstituted soils at high initial water contents. *Geotechnique*, *60*(9), 691–700. https://doi.org/10.1680/geot.09.P.059

Hu, K., Chai, Z., Whitesell, J. K., & Bard, A. J. (1999). In situ monitoring of diffuse double layer structure changes of electrochemically addressable self-assembled monolayers with an atomic force microscope. *Langmuir*, *15*(9), 3343–3347. https://doi.org/10.1021/la9813937

Hueckel, T. A. (1992). Water mineral interaction in hygromechanics of clays exposed to environmental loads—A mixture-theory approach. *Canadian Geotechnical Journal*, *29*(6), 1071–1086. https://doi.org/10.1139/t92-124

Hyodo, M., Wu, Y., Kajiyama, S., Nakata, Y., & Yoshimoto, N. (2017). Effect of fines on the compression behaviour of poorly graded silica sand. *Geomechanics and Engineering*, *12*(1), 126–138.

Israelachvili, J. N. (2011). *Intermolecular and surface forces*. San Diego, CA: Academic Press.

Jang, J., Cao, S. C., Stern, L. A., Waite, W. F., & Jung, J. (2018). Effect of pore fluid chemistry on the sedimentation and compression behavior of pure, endmember fines. U.S Geological Survey Data Release. https://doi.org/10.5066/F77M076K

Jang, J., & Santamarina, J. C. (2016). Fines classification based on sensitivity to pore-fluid chemistry. *Journal of Geotechnical and Geoenvironmental Engineering*, *142*(4), 06015018. https://doi.org/10.1061/(ASCE)GT.1943-5606.0001420

Jang, J., & Santamarina, J. C. (2017). Closure to "Fines classification based on sensitivity to pore-fluid chemistry" by Junbong Jang and J. Carlos Santamarina. *Journal of Geotechnical and Geoenvironmental Engineering*, *143*(7), 07017013. https://doi.org/10.1061/(ASCE)GT.1943-5606.0001694

Kenney, T. C. (1977). Residual strength of mineral mixtures. *Proceedings 9th International Conference on Soil Mechanics and Foundation Engineering*, Oslo, Norway. 1, 123–129.

Kopf, A. J., Kasten, S., & Blees, J. (2010). Geochemical evidence for groundwater-charging of slope sediments: The Nice Airport 1979 landslide and tsunami. In D. C. Mosher, R. C. Shipp, L. Moscardelli, J. D. Chaytor, C. D. P. Baxter, H. J. Lee, & R. Urgeles (Eds.), *Submarine mass movements and their consequences* (pp. 203–214). New York: Springer.

Kurihara, M., Funatsu, K., Ouchi, H., Sato, A., Yasuda, M., Narita, H., et al. (2011). Analysis of 2007/2008 JOGMEC/NRCAN/AURORA Mallik gas hydrate production test through numerical simulation. *The 7th International Conference on Gas Hydrates (ICGH 2011)*, Edinburgh, Scotland, United Kingdom.

Kurihara, M., Sato, A., Funatsu, K., Ouchi, H., Masuda, Y., Narita, H., & Collett, T. S. (2011). Analysis of formation pressure test results in the Mount Elbert methane hydrate reservoir through numerical simulation. *Marine and Petroleum Geology*, *28*(2), 502–516. https://doi.org/10.1016/j.marpetgeo.2010.01.007

Kvenvolden, K. A. (1988). Methane hydrate—A major reservoir of carbon in the shallow geosphere. *Chemical Geology*, *71*(1–3), 41–51. https://doi.org/10.1016/0009-2541(88)90104-0

Lade, P. V., & Yamamuro, J. A. (1997). Effects of nonplastic fines on static liquefaction of sands. *Canadian Geotechnical Journal*, *34*(6), 918–928. https://doi.org/10.1139/t97-052

Lagaly, G. (1989). Principles of flow of kaolin and bentonite dispersions. *Applied Clay Science*, *4*(2), 105–123. https://doi.org/10.1016/0169-1317(89)90003-3

Lambe, T. W., & Whitman, R. V. (1969). *Soil mechanics*. New York: John Wiley.

Langmuir, I. (1938). The role of attractive and repulsive forces in the formation of tactoids, thixotropic gels, protein crystals and coacervates. *Journal of Chemical Physics*, *6*, 873–896.

Leblanc, D. R., Garabedian, S. P., Hess, K. M., Gelhar, L. W., Quadri, R. D., Stollenwerk, K. G., & Wood, W. W. (1991). Large-scale natural gradient tracer test in sand and gravel, cape-cod, Massachusetts:1. Experimental-design and observed tracer movement. *Water Resources Research*, *27*, 895–910. https://doi.org/10.1029/91WR00241

Lee, J. M., Shackelford, C. D., Benson, C. H., Jo, H. Y., & Tuncer, B. E. (2005). Correlating index properties and hydraulic conductivity of geosynthetic clay liners. *Journal of Geotechnical and Geoenvironmental Engineering*, *131*(11), 1319–1329. https://doi.org/10.1061/(ASCE)1090-0241(2005)131:11(1319)

Mackay, D. M., & Cherry, J. A. (1989). Groundwater contamination—Pump-and-treat remediation: 2. *Environmental Science & Technology*, *23*(6), 630–636. https://doi.org/10.1021/es00064a001

McBride, M. B., & Baveye, P. (2002). Diffuse double-layer models, long-range forces, and ordering in clay colloids. *Soil Science Society of America Journal*, *66*(4), 1207–1217. https://doi.org/10.2136/sssaj2002.1207

Meade, R. H. (1964). Rearrangement of particles during the compaction of clayey sediments—Review. Geological Survey Professional Paper 497-B. United States Government Printing Office, Washington.

Meier, L. P., & Kahr, G. (1999). Determination of the cation exchange capacity (CEC) of clay minerals using the complexes of copper (II) ion with triethylenetetramine and tetraethylenepentamine. *Clays and Clay Minerals*, *47*(3), 386–388. https://doi.org/10.1346/CCMN.1999.0470315

Mitchell, J. K., & Soga, K. (2005). *Fundamentals of soil behavior*. New York: John Wiley.

Mohan, K. K., Vaidya, R. N., Reed, M. G., & Fogler, H. S. (1993). Water sensitivity of sandstones containing swelling and non-swelling clays. *Colloids and Surfaces a-Physicochemical and Engineering Aspects*, *73*, 237–254.

Mojid, M. A., & Cho, H. (2006). Estimating the fully developed diffuse double layer thickness from the bulk electrical conductivity in clay. *Applied Clay Science*, *33*(3–4), 278–286. https://doi.org/10.1016/j.clay.2006.06.002

Moore, C. A., & Mitchell, J. K. (1974). Electromagnetic forces and soil strength. *Geotechnique*, *24*(4), 627–640. https://doi.org/10.1680/geot.1974.24.4.627

Moridis, G. J., & Reagan, M. T. (2007a). Gas production from oceanic class 2 hydrate accumulations. *Offshore Technology Conference*, Houston, Texas, 30 April - 3 May, 2007. OTC 18866.

Moridis, G. J., & Reagan, M. T. (2007b). Strategies for gas production from oceanic class 3 hydrate accumulations. *Offshore Technology Conference*, Houston, Texas, 30 April - 3 May, 2007. OTC 18865.

Van Olphen, H. (1977). *An introduction to clay colloid hemistry*. New York: John Wiley.

Olson, R. E., & Mesri, G. (1970). Mechanisms controlling compressibility of clays. *Journal of Soil Mechanics and Foundations Division, Proceedings of the American Society of Civil Engineers*, *96*(SM6), 1863–1878.

Oyama, H., Abe, S., Yoshida, T., Sato, T., Nagao, J., Tenma, N., & Narita, H. (2016). Experimental study of mud erosion at the interface of an artificial sand-mud alternate layer. *Journal of Natural Gas Science and Engineering*, *34*, 1106–1114. https://doi.org/10.1016/j.jngse.2016.07.067

Palomino, A. M., & Santamarina, J. C. (2005). Fabric map for kaolinite: Effects of pH and ionic concentration on behavior. *Clays and Clay Minerals*, *53*(3), 209–222.

Park, J., & Santamarina, J. C. (2017). Revised soil classification system for coarse-fine mixtures. *Journal of Geotechnical and Geoenvironmental Engineering*, *143*(8), 04017039. https://doi.org/10.1061/(ASCE)GT.1943-5606.0001705

Petschick, R., Kuhn, G., & Gingele, F. (1996). Clay mineral distribution in surface sediments of the South Atlantic: Sources, transport, and relation to oceanography. *Marine Geology*, *130*(3–4), 203–229. https://doi.org/10.1016/0025-3227(95)00148-4

Piekarski, K., & Munro, M. (1977). Transport mechanism operating between blood-supply and osteocytes in long bones. *Nature*, *269*(5623), 80–82. https://doi.org/10.1038/269080a0

Pierre, A. C., & Ma, K. (1999). DLVO theory and clay aggregate architectures formed with AlCl3. *Journal of the European Ceramic Society*, *19*(8), 1615–1622. https://doi.org/10.1016/S0955-2219(98)00264-7

Priest, J. A., Druce, M., Roberts, J., Schultheiss, P., Nakatsuka, Y., & Suzuki, K. (2015). PCATS Triaxial: A new geotechnical apparatus for characterizing pressure cores from the Nankai Trough, Japan. *Marine and Petroleum Geology*, *66*, 460–470. https://doi.org/10.1016/j.marpetgeo.2014.12.005

Pudlo, D., Henkel, S., Reitenbach, V., Albrecht, D., Enzmann, F., Heister, K., et al. (2015). The chemical dissolution and physical migration of minerals induced during CO_2 laboratory experiments: Their relevance for reservoir quality. *Environmental Earth Sciences*, *73*(11), 7029–7042. https://doi.org/10.1007/s12665-015-4411-x

Quirk, J. P., & Schofield, R. K. (1955). The effect of electrolyte concentration on soil permeability. *Journal of Soil Science*, *6*(2), 163–178. https://doi.org/10.1111/j.1365-2389.1955.tb00841.x

Rao, P. S. C., Annable, M. D., Sillan, R. K., Dai, D. P., Hatfield, K., Graham, W. D., et al. (1997). Field-scale evaluation of in situ cosolvent flushing for enhanced aquifer remediation. *Water Resources Research*, *33*, 2673–2686. https://doi.org/10.1029/97WR02145

Ripmeester, J. A., Lu, H., Moudrakovski, I. L., Dutrisac, R., Wilson, L. D., Wright, F., & Dallimore, S. R. (2005). Structure and composition of gas hydrate in sediment recovered from the JAPEX/JNOC/GSC et al. Mallik 5L-38 gas hydrate production research well, determined by X-ray diffraction and Raman and solid-state nuclear magnetic resonance spectroscopy. *Scientific Results from the Mallik 2002 Gas Hydrate Production Research Well* Program*, Mackenzie Delta, Northwest Territories, Canada*. S. R. Dallimore and T. S. Collett, Geological Survey of Canada, Bulletin 585.

Ruppel, C. D., & Kessler, J. D. (2017). The interaction of climate change and methane hydrates. *Reviews of Geophysics*, *55*(1), 126–168. https://doi.org/10.1002/2016RG000534

Santamarina, J. C., Dai, S., Terzariol, M., Jang, J., Waite, W. F., Winters, W. J., et al. (2015). Hydro-bio-geomechanical properties of hydrate-bearing sediments from Nankai Trough. *Marine and Petroleum Geology*, *66*, 434–450. https://doi.org/10.1016/j.marpetgeo.2015.02.033

Santamarina, J. C., Klein, K. A., & Fam, M. A. (2001). *Soils and Waves*. New York: John Wiley.

Santamarina, J. C., Klein, K. A., Wang, Y. H., & Prencke, E. (2002). Specific surface: Determination and relevance. *Canadian Geotechnical Journal*, *39*(1), 233–241. https://doi.org/10.1139/t01-077

Schultheiss, P., Holland, M., Roberts, J., Huggett, Q., Druce, M., & Fox, P. (2011). PCATS: Pressure core analysis and transfer system. The 7th International Conference on Gas Hydrates, Edinburgh, Scotland, United Kingdom.

Skempton, A. W., & Northey, R. D. (1953). The sensitivity of clays. *Geotechnique*, *3*(1), 30–53.

Sloan, E. D., & Koh, C. A. (2007). *Clathrate Hydrates of Natural Gases*. New York: CRC Press, Taylor & Francis Group, LLC.

Sloan, E. D., & Koh, C. A. (2008). *Clathrate hydrates of natural gases*. New York: CRC Press, Taylor & Francis Group, LLC.

Sogami, I. (1983). Effective potential between charged spherical-particles in dilute suspension. *Physics Letters A*, *96*(4), 199–203. https://doi.org/10.1016/0375-9601(83)90704-1

Sogami, I., & Ise, N. (1984). On the electrostatic interaction in macroionic solutions. *The Journal of Chemical Physics*, *81*(12), 6320–6332. https://doi.org/10.1063/1.447541

Sposito, G. (1989). *The chemistry of soils*. New York: Oxford University Press.

Sridharan, A., & Nagaraj, H. B. (2000). Compressibility behaviour of remoulded, fine-grained soils and correlation with index properties. *Canadian Geotechnical Journal*, *37*(3), 712–722. https://doi.org/10.1139/t99-128

Sridharan, A., & Rao, G. V. (1973). Mechanisms controlling volume change of saturated clays and role effective stress concept. *Geotechnique*, *23*(3), 359–382. https://doi.org/10.1680/geot.1973.23.3.359

Stumm, W. (1992). *Chemistry of the solid-water interface: Processes at the mineral-water and particle-water interface in natural systems*. New York: John Wiley.

Sultan, N., Cochonat, P., Canals, M., Cattaneo, A., Dennielou, B., Haflidason, H., et al. (2004). Triggering mechanisms of slope instability processes and sediment failures on continental margins: A geotechnical approach. *Marine Geology*, *213*(1–4), 291–321. https://doi.org/10.1016/j.margeo.2004.10.011

Sun, X. L., & Turchyn, A. V. (2014). Significant contribution of authigenic carbonate to marine carbon burial. *Nature Geoscience*, *7*(3), 201–204. https://doi.org/10.1038/ngeo2070

Tanaka, H., & Locat, J. (1999). A microstructural investigation of Osaka Bay clay: The impact of microfossils on its mechanical behaviour. *Canadian Geotechnical Journal*, *36*(3), 493–508. https://doi.org/10.1139/t99-009

Tiwari, B., & Ajmera, B. (2011). Consolidation and swelling behavior of major clay minerals and their mixtures. *Applied Clay Science*, *54*(3–4), 264–273. https://doi.org/10.1016/j.clay.2011.10.001

Uchida, S., Lin, J. S., Myshakin, E., Seol, Y., Collett, T. S., & Boswell, R. (2017). Numerical simulations of sand production in interbedded hydrate-bearing sediments during depressurization. *The 9th International Conference on Gas Hydrates*, Denver, Colorado, USA, June 25–30, 2017.

Uddin, M., Wright, J. F., Dallimore, S. R., & Coombe, D. (2012). Gas hydrate production from the Mallik reservoir: Numerical history matching and long-term production forecasting. *Scientific results from the JOGMEC/NRCan/Aurora Mallik 2007–2008 gas hydrate production research well* Program*, Mackenzie Delta, Northwest Territories, Canada*. S. R. Dallimore, K. Yamamoto, J. F. Wright and G. Bellefleur, Geological Survey of Canada, Bulletin 601, 261–289.

Valdes, J. R., & Santamarina, J. C. (2007). Particle transport in a nonuniform flow field: Retardation and clogging. *Applied Physics Letters*, *90*(24), 244101. https://doi.org/10.1063/1.2748850

Valle-Delgado, J. J., Molina-Bolivar, J. A., Galisteo-Gonzalez, F., Galvez-Ruiz, M. J., Feiler, A., & Rutland, M. W. (2005). Hydration forces between silica surfaces: Experimental data and predictions from different theories. *Journal of Chemical Physics*, *123*(3), 034708. https://doi.org/10.1063/1.1954747

Verwey, E. J. W., Overbeek, J. T. G., & Nes, K. V. (1948). *Theory of the stability of lyophobic colloids: The interactions of sol particles having an electric double layer*. New York: Elsevier Pub. Co.

Vitagliano, V., & Lyons, P. A. (1956). Diffusion coefficients for aqueous solutions of sodium chloride and barium chloride. *Journal of the American Chemical Society*, *78*(8), 1549–1552. https://doi.org/10.1021/ja01589a011

Wang, L. Y., Cowin, S. C., Weinbaum, S., & Fritton, S. P. (2000). Modeling tracer transport in an osteon under cyclic loading. *Annals of Biomedical Engineering*, *28*(10), 1200–1209. https://doi.org/10.1114/1.1317531

Wiemer, G., Dziadek, R., & Kopf, A. (2017). The enigmatic consolidation of diatomaceous sediment. *Marine Geology*, *385*, 173–184. https://doi.org/10.1016/j.margeo.2017.01.006

Winters, W., Walker, M., Hunter, R., Collett, T., Boswell, R., Rose, K., et al. (2011). Physical properties of sediment from the Mount Elbert gas hydrate stratigraphic test well, Alask North Slope. *Marine and Petroleum Geology*, *28*(2), 361–380. https://doi.org/10.1016/j.marpetgeo.2010.01.008

Wroth, C. P., & Wood, D. M. (1978). The correlation of index properties with some basic engineering properties of soils. *Canadian Geotechnical Journal*, *15*(2), 137–145. https://doi.org/10.1139/t78-014

Xu, W. Y., & Ruppel, C. (1999). Predicting the occurrence, distribution, and evolution of methane gas hydrate in porous marine sediments. *Journal of Geophysical Research*, *104*, 5081–5095. https://doi.org/10.1029/1998JB900092

Yamamoto, K., Kanno, T., Wang, X. X., Tamaki, M., Fujii, T., Chee, S. S., et al. (2017). Thermal responses of a gas hydrate-bearing sediment to a depressurization operation. *RSC Advances*, *7*(10), 5554–5577. https://doi.org/10.1039/C6RA26487E

Yamamoto, K., Terao, Y., Fujii, T., Ikawa, T., Seki, M., & Matsuzawa, M. (2014). Operational overview of the first offshore production test of methane hydrates in the Eastern Nankai Trough. *Offshore Technology Conference*, OTC 25243.

Yoneda, J., Masui, A., Konno, Y., Jin, Y., Egawa, K., Kida, M., et al. (2015). Mechanical behavior of hydrate-bearing pressure-core sediments visualized under triaxial compression. *Marine and Petroleum Geology*, *66*, 451–459. https://doi.org/10.1016/j.marpetgeo.2015.02.028

Yoneda, J., Masui, A., Konno, Y., Jin, Y., Kida, M., Katagiri, J., et al. (2017). Pressure-core-based reservoir characterization for geomechanics: Insights from gas hydrate drilling during 2012-2013 at the eastern Nankai Trough. *Marine and Petroleum Geology*, *86*, 1–16. https://doi.org/10.1016/j.marpetgeo.2017.05.024

Zatsepina, O. Y., & Buffett, B. A. (1997). Phase equilibrium of gas hydrate: Implications for the formation of hydrate in the deep sea floor. *Geophysical Research Letters*, *24*, 1567–1570. https://doi.org/10.1029/97GL01599